Automated far-field sound field estimation combining robotized acoustic measurements and the boundary elements method

Caroline Pascal, Pierre Marchand, Alexandre Chapoutot, Olivier Doaré

Automated far-field sound field estimation combining robotized acoustic measurements and the boundary elements method

Caroline Pascal,[1, a] Pierre Marchand,[2] Alexandre Chapoutot,[3] and Olivier Doaré[4]

[1] *UME and U2IS, ENSTA Paris, Institut Polytechnique de Paris*

828 Boulevard des Maréchaux, 91120 Palaiseau, France

[2] *POEMS, CNRS, Inria, ENSTA Paris, Institut Polytechnique de Paris*

828 Boulevard des Maréchaux, 91120 Palaiseau, France

[3] *U2IS, ENSTA Paris, Institut Polytechnique de Paris*

828 Boulevard des Maréchaux, 91120 Palaiseau, France

[4] *UME, ENSTA Paris, Institut Polytechnique de Paris*

828 Boulevard des Maréchaux, 91120 Palaiseau, France

The identification and reconstruction of acoustic fields radiated by unknown structures is usually performed using either Sound Field Estimation (SFE) or Near-field Acoustic Holography (NAH) techniques. The latter turns out to be especially useful when data is only available close to the source, but information throughout the whole space is needed.

Yet, the lack of amendable and efficient implementations of state-of-the-art solutions, as well as the laborious and often lengthy deployment of acoustic measurements continue to be significant obstacles to the practical application of such methods.

The purpose of this work is to address both problems. First, a completely automated metrology setup is proposed, in which a robotic arm is used to gather extensive, yet accurate geometric and acoustic data without any human intervention. The impact of the robot on acoustic pressure measurements has been cautiously estimated, and proved to remain negligible within a defined validity frequency range.

The sound field prediction is then tackled using the Boundary Element Method (BEM), and implemented using the *FreeFEM++* BEM library. Numerically simulated measurements have allowed us to assess the method accuracy, which matches theoretically expected results, and robustness against positioning inaccuracies, provided that the robot is carefully calibrated.

The overall solution has been successfully tested using actual robotized measurements of an unknown loudspeaker, with a reconstruction error of less than 30 % on the previously defined validity frequency range.

[a]caroline.pascal.2020@ensta-paris.fr

I. INTRODUCTION

The reconstruction of the acoustic pressure field radiated by an arbitrary source, using only a limited set of actual microphone measurements, is a common task in experimental acoustics. In particular, *Sound Field Estimation* (SFE) aims to accurately predict the far-field properties of a studied source based on near-field measurements. In that way, it is possible to study the impact of the source in its environment, without having to perform wide range measurements at a large distance from the source. This method has proven to be relevant for loudspeaker characterization (Klippel, 2022), but also for the study of other noise sources, such as aircraft (Martinus *et al.*, 2005), UAVs (Bi *et al.*, 2021), cars (Wu and Wu, 1998) (Gade *et al.*, 2014) (Tao and Ren, 2010) or trains (Wang and Bei, 2017) to cite a few.

On the other hand, *Near-field Acoustic Holography* (NAH) objective is to estimate the surfacic acoustic features of a radiating source using near-field measurements. Unlike SFE, NAH tries to solve an inverse problem, and requires an additional regularization step. Yet, NAH algorithms may also be used to solve SFE problems (Salin and Kosteev, 2020), and will equivalently be considered in the following.

The foundations of SFE and NAH rely on two main aspects: the practical acoustic measurements, and the reconstruction method.

a. Acoustic measurements. One of the main challenges encountered while performing SFE acoustic measurements is the need to perform numerous accurately positioned, near-field measurements.

Traditionally, this issue has been tackled by the use of microphone arrays, consisting of a rigid assembly of microphones, which can be fixed at a given distance from the source. Such arrays come in various geometries - linear (Gur, 2014), planar (Hald *et al.*, 2008) (Li *et al.*, 2021), (Wang and Bei, 2017), cylindrical (Norris, 1997) (Su *et al.*, 2017) (Gur, 2017), spherical (Bi *et al.*, 2021) (Behler *et al.*, 2012) - but often lack of versatility, as their cost makes it is not foreseeable to create a new array for each studied object. Furthermore, the simultaneous operation of many microphones requires adapted, expensive hardware, as well as a careful calibration of the array (Sugiyama *et al.*, 2023).

In order to allow variable resolution and large-scale measurements, the idea of mobile arrays have been quickly introduced: rigid arrays are mounted on one (Havranek *et al.*, 2015), two (De La Croix *et al.*, 2005) or three (Szczodrak *et al.*, 2016) (Virovlyansky and Deryabin, 2019) prismatic joints, or one revolute joint (McBride *et al.*, 2020) (Vold *et al.*, 2010), and moved around the source to gather the required data. Yet, depending on the axes' layout, some positions and orientations of the microphones remain unreachable.

Recent work have proposed to combine motion tracking (Luo *et al.*, 2021) (Fernandez Comesana *et al.*, 2015), 2D (Legg and Bradley, 2013) and 3D (Meyer and Döbler, 2006) (Li *et al.*, 2021) (Legg and Bradley, 2014) localization methods with acoustic measurements, so that the microphone, or microphone array, is continuously located during the process. If such approaches lead to a greater versatility and the ability to perform measurements at a larger scale, they are still limited by occlusion issues, and does not enable fully autonomous measurements.

Eventually, the use of multiple degrees of freedom robots for acoustic measurements has been considered, with for instance the robotized NAH solution proposed by Klippel Klippel and Bellmann (2016), using a cylindrical robot with 3 *Degrees Of Freedom* (DOF).

The use of full 6 DOF robots in acoustic however still remains scarce, with few applications in non-destructive testing (Bernhardt *et al.*, 2020) (Walker and Foged, 2018), room acoustics (Nolan *et al.*, 2019), and NAH (Kefer and Lu, 2016) (Knežević *et al.*, 2018). However, most of these procedures still limit themselves to planar measurements, and are not taking the full benefits of the maneuverability and autonomy of the robot. Furthermore, the actual impact of the robot on the measurements, both in terms of positioning accuracy (Pascal *et al.*, 2023) and acoustic footprint, remains to be assessed.

b. Sound field estimation. In its most generic form, SFE allows for a temporal as well as a spatial estimation of the sound field, that is, the sought acoustic quantity is expressed as a function of both space and time. In our case however, we will assume that the studied source is stationary, and that the sound field is only a function of space, with a harmonic time dependency.

As for most identification problems, SFE relies on two major steps: modeling and identification. The modeling step essentially translates the way the sound field is represented. Two options were mainly investigated in the literature: the sound field may be written as an expansion of elementary solutions of the Helmhotz equation, or as a solution of this equation, identified over a given discretized function space.

The first approach was originally investigated by Maynard *et al.* (1985), using a *Spatial Fourier Transform* (SFT) method. It however suffers from a lack of flexibility, as the el-

ementary solutions are limited to a few simple separable geometries, and is impacted by aliasing effects.

The expansion approach has then been intensively investigated in order to cope with SFT issues. The *Statistically Optimized NAH* (SONAH) method proposed by Hald (2009), dealt with the frequential aliasing issue with a continuous approach of the wave-number space. The *Helmholtz Equation Least Squares* (HELS) method proposed by Wu (2000) and Wu (2015) opted for spheroidal elementary solutions as the expansion set. The *Equivalent Source Method* (ESM) (Valdivia, 2019) proposed a more tangible modeling approach, using isolated and distributed (Semenova and Wu, 2005) artificial sources as elementary solutions. In particular, the spherical harmonics expansion (Klippel, 2022) uses punctual acoustic sources, defined by a finite sum of spherical harmonics, which allows for an accurate reconstruction of the sound field with a limited expansion set. Yet, in the end, all these methods require i) a clever choice of expansion set (Canclini *et al.*, 2017) (Antoni, 2012) and ii) a discretization choice on this set to ensure a good trade-off between reconstruction accuracy, computational resources and the risk of over-fitting (Chardon *et al.*, 2013) (Semenova and Wu, 2005).

The identification of the expansion coefficients is often performed using a least-squares approach, combined with a regularization scheme to ensure the reconstruction regularity, especially when solving NAH problems (Williams, 2001) (Martinus *et al.*, 2007). Recent developments, benefitting from the compressive sensing theory, have proposed a sparse identification of the expansion coefficients (Hald, 2016), in order to avoid the energy spreading effect caused by an L^2 norm minimization. An L^0 or L^1 norm minimization (Chardon *et al.*, 2012) (Hald, 2018) indeed leads to a concentration of the energy on a few expansion func-

tions, or artificial sources, hence allowing for a better reconstruction accuracy far from the measurements.

On the other hand, several work opted for a direct resolution of the Helmholtz equation, using an element-based approach. Whereas the *Finite Elements Method* (FEM) (Ungnad and Sachau, 2019) received small attention, mainly because of its impractical adaptation to infinite domains and pollution effects, most efforts were put on the *Boundary Elements Method* (BEM) (Bai, 1992) (Kim and Ih, 1996) (Martinus *et al.*, 2007) (Herrin *et al.*, 2010) (Bi *et al.*, 2019) (Luo *et al.*, 2021). In comparison to the expansion approach, BEM offers a higher flexibility, as the only requirement is that measurements are to be performed on the nodes of a surfacic mesh. In particular, the impact of the choice of the discretized function space can be predicted *a priori*, and the method is not impacted by frequential aliasing, or by the placement of artificial sources. However, such flexibility comes at a cost, as computations are inherently more complex, and resources consuming.

It should be noted that the recent emergence of learning-based methods in physics-based problems have led to the use of convolutional (Alguacil *et al.*, 2021) and physics informed (Chen *et al.*, 2023) (Olivieri *et al.*, 2021) (Shigemi *et al.*, 2022) neural networks to solve the SFE problem. Although these methods have shown promising results, they are still limited by the need of a large amount of data, and the lack of physical guarantees and interpretations of the results.

Despite their great diversity, all these methods still remain scarcely implemented, especially in open-source software, and often prove to be poorly coupled with the actual measurements step.

c. Problem statement. The practical setup of SFE tools is hindered by two major drawbacks: the lack of efficient implementation of the existing numerical methodologies, and the time-consuming and tedious roll-out of acoustic measurements.

d. Contributions. We present a novel acoustic sound field estimation methodology, handling both the measurements and reconstruction steps. The measurements are performed using a 7 DOF arm robot, allowing for numerous and versatile measurements, and the reconstruction is performed using an optimized parallel implementation of BEM (Hecht, 2012)(Marchand, 2020). Bearing in mind that the quality of a metrology system depends on the impact of each item in the acquisition chain, the actual impact of the robot on the measurements is assessed, and the underlying effects on the reconstructed sound field are discussed.

II. ACOUSTIC ROBOTIZED MEASUREMENTS

One of the main contribution of this paper is the introduction of a robotic arm to perform accurate tri-dimensional acoustic measurements in full autonomy. The details of the experimental setup, and the impact of the robot on the measurements are presented in this section.

A. Measurements setup

Drawing inspiration from previous works (Walker and Foged, 2018) (Nolan *et al.*, 2019) (Knežević *et al.*, 2018), we designed a complete measurement setup (*cf.* Fig. 1) combining a Franka Robotics Panda serial robot, equipped with a numerically manufactured microphone

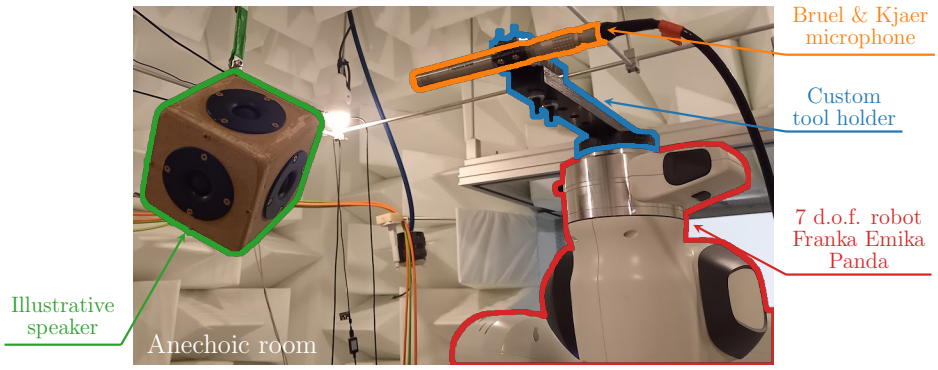

FIG. 1. Robotized acoustic measurements setup.

prop, allowing the microphone to be held at a distance from the robot while performing the measurements. The 7 degrees of freedom of the serial robot allow for an increased maneuverability and a simplified collision avoidance, by offering multiple possible configurations for the same microphone position and orientation.

The handling of the robot inverse kinematics and motion planning computation is overseen by the Moveit (Coleman *et al.*, 2014) library implemented in *Robot Operating System* (ROS) (Quigley *et al.*, 2009), which hand fully bypasses the impractical proprietary software. This library also offers off-the-shelf tools for self and external collision avoidance, and supports the addition of geometric constraints during inverse kinematics resolution. The latter asset was successfully exploited to free an additional degree of freedom associated to the rotation around the microphone axis, which does not impact the measurement.

On the microphone side, the support tool was designed to fit most Bruel & Kjaer and GRAS microphone pre-amplifiers. The acoustic measurements are handled by the *measpy* (Doaré, 2024) Python library, which generically handles signals provided by classical sound cards, and National Instruments acquisition devices. In our current set up, a Bruel & Kjaer

4190 free-field microphone mounted on a GRAS 26AJ preamplifier were used, and recorded using a Behringer UMC404HD sound card.

All features were finally bundled up in a single ROS package *robot_arm_acoustics* (Pascal, 2024), allowing to easily define the robotic cell collisions objects, and plan autonomous measurements routines along generic trajectories (circles, spheres, lines, etc.).

B. Robotized measurements validity hypothesis

The advantages in versatility and autonomy of the robotized measurements setup comes at the cost of a more complex measurement processing and inherently bulkier installation. To ensure the measurements quality, three hypotheses are derived, and assessed.

a. Hypothesis 1: Time-invariant sound source. In comparison to usual microphone-array-based measurements setups, where all acquisitions are performed simultaneously, robotized acoustic measurements are performed sequentially. As our work focuses on the study of electroacoustic measurements, where the response to an input signal is measured, this lack of synchronicity is not a problem as long as the transfer function between these correlated signals is computed.

In particular, our focus is set on the estimation of the sound field radiated by a JBL FLip 2, which was monaurally fed on its left channel with a white noise signal of 10 seconds, containing frequencies between $f_{min} = 10$ Hz and $f_{max} = 20$ kHz. The transfer functions between the recorded acoustic pressure (in Pa), and the signal generated by the sound card (in V) were then computed using the Welch (1967) method, and smoothed over 1/12 octave bands.

Additionally, the behavior of the studied sound source must remain the same throughout the whole characterization process, by generating the same output signal for a given input signal. In other words, any measurement at a given location must generate the same results, regardless to the time at which it was performed. As this hypothesis heavily depends on the studied source, it was assessed experimentally by performing a series of three consecutive measurements with the robot fixed in the same configuration (*cf.* first configuration on Fig. 3).

The obtained transfer functions and the corresponding modulus errors are displayed on Fig. 2. The error between two complex transfer functions H_1 and H_2 is expressed as the logarithm of the modulus and phase of their ratio:

$$\epsilon(H_1, H_2) = \left(20 \log\left(\frac{|H_1|}{|H_2|}\right), \arg(H_1 - H_2)\right),$$

where H_2 is the reference transfer function, and in our case, the first transfer function of the series.

As expected from an industrial product, the loudspeaker features a good time invariability, with an average error of 0.25 dB over the whole frequency range. Consequently, the hypothesis of a time-invariant sound source is considered verified for the studied loudspeaker.

b. Hypothesis 2: Low robot acoustic footprint. As the robot is not an acoustic transparent element, it will inherently impact the acoustic measurements. Although parasitic noise generated by the robot can be filtered during the transfer function computation, thanks to averaged measurements over a sufficiently long period of time (Welch, 1967), the robot acoustic footprint is more complex to handle, as it depends on the robot angular configuration.

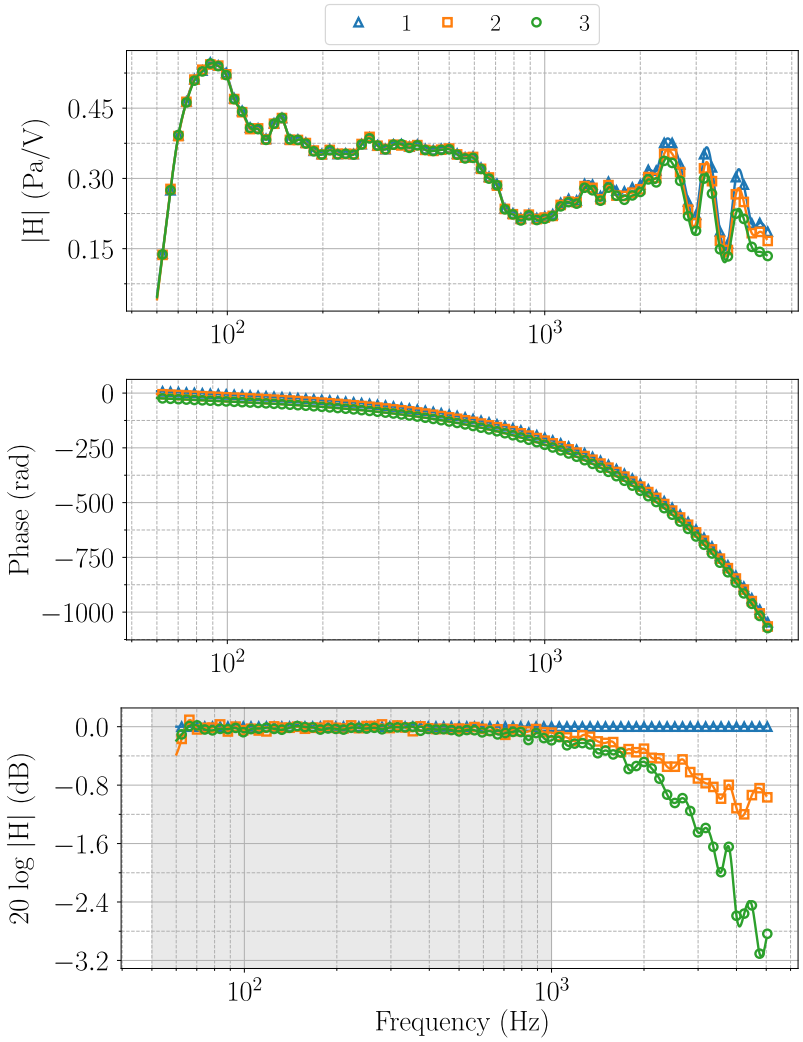

FIG. 2. Time-invariability results obtained for the JBL FLip 2, with the robot set in the first control configuration of Fig. 3. The first two plots represent the computed transfer functions, and the last one the modulus error relative to the first (1) transfer function. The shaded zone highlights the frequency range where the absolute value of the error remains below 0.25 dB.

As for the time invariability, our aim was to experimentally assess that the robot acoustic footprint is actually low enough to be neglected in the following. To achieve so, we performed two successive series of acoustic measurements, with the microphone rigidly held in the same position using pliers. For the first series, the robot is moved aside, so that its presence

does not impact the acquisition. For the second one, it is placed as if it was holding the microphone in the very same position. As the microphone and its fixations are not shifted between the two series of measurements, their difference will only depend on the acoustic impact of the robot.

These two-fold series of measurements were performed at six so-called control configurations located around a JBL Flip 2, and are displayed on Fig. 3.

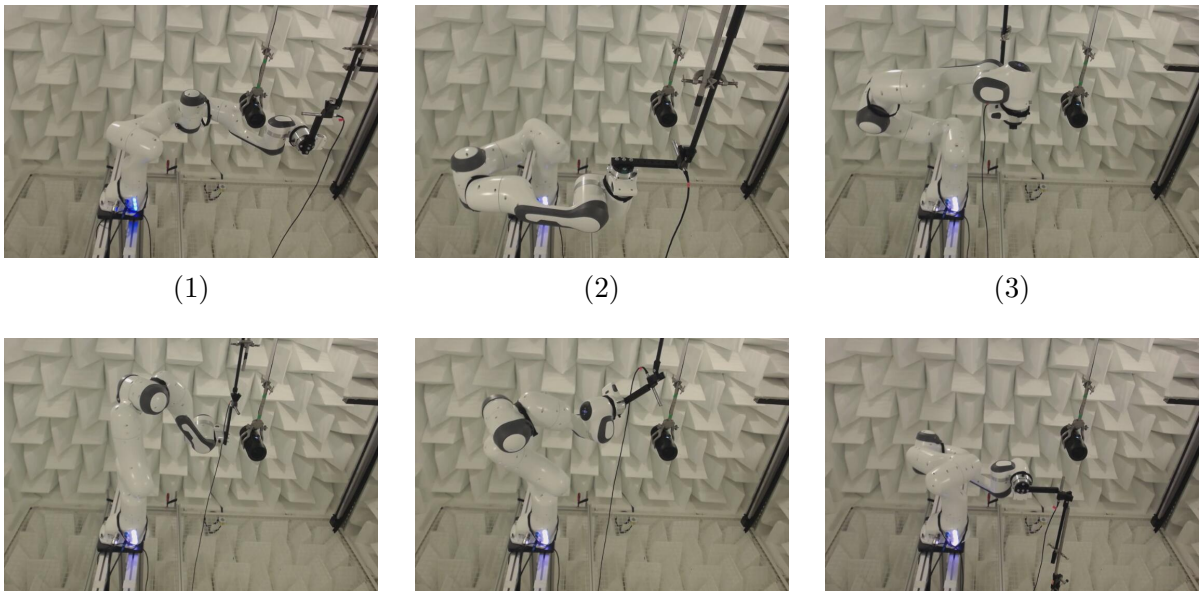

FIG. 3. Robot control configurations for sound source time invariance and robot acoustic footprint assessment.

For each control configuration, the error between the transfer functions obtained with and without the robot is displayed on Fig. 4.

Unlike the time-invariability results, the robot acoustic footprint has a non-negligible impact on the measurements, especially at higher frequencies. Yet, such behavior was expected: at lower frequencies, and larger wavelengths, the robot becomes small enough not

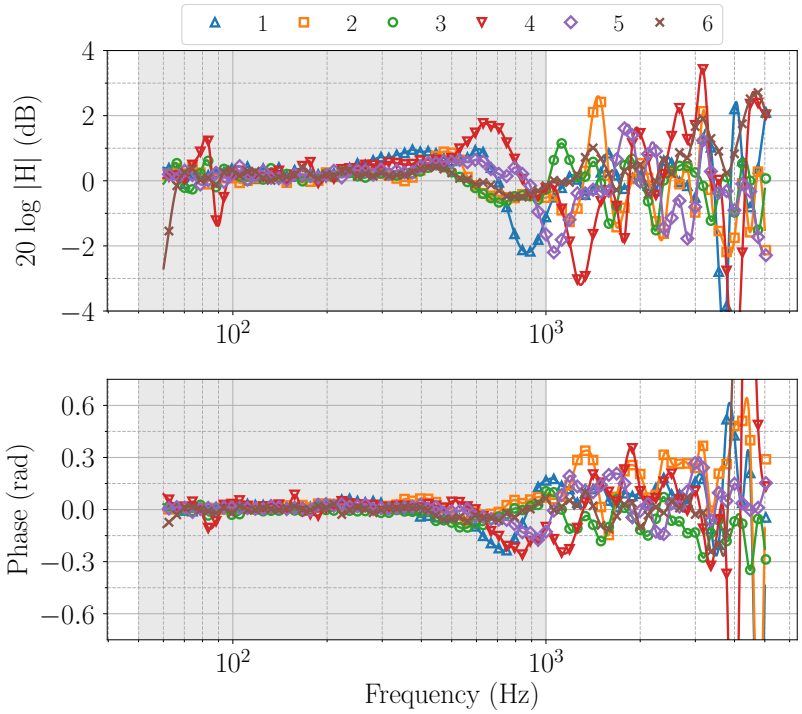

FIG. 4. Robot acoustic footprint errors obtained for the six robot control configurations, relative to the robot-less transfer function. The shaded zone highlights the frequency range where the absolute value of the modulus error remains below 2.25 dB.

to disturb the sound propagation. On the other hand, at higher frequencies and smaller wavelengths, the robot becomes a significant obstacle, and generates reflections of the incoming waves towards the microphone. As seen on Fig. 4, this behavior becomes globally noticeable above $f = 500$ Hz, which corresponds to a wavelength of $\lambda = 0.68$ m, and is consistent with the robot dimensions. More specifically, configurations (1) and (4) appear to be the most impactful, as the robot is the closest and most exposed to the sound source. Inversely, configurations (2) and (6) have a lower impact on the measurements, as the robot is further away from the source, and exposes a smaller surface to the incoming waves.

Nevertheless, the deterioration caused by the robot induced reflections remain under an acceptable level for frequencies below $f = 1$ kHz, with an amplitude error below 2.25 dB and a phase difference of 0.25 rad at its maximum, as shown on Fig. 4. As the sounds generated by the loudspeaker become actually significant only above $f = 50$ Hz, the frequency range $[50\ Hz, 1\ \text{kHz}]$ will be defined as the validity frequency range for our setup, within which measurements will be considered exploitable.

c. Hypothesis 3: Low robot positioning error. Although robotic arms are known for their high repeatability and maneuverability, their flawed accuracy is often disregarded when used for metrology purposes. In this context however, an accurate sensor placement is of paramount importance (Martinus *et al.*, 2007), as it directly impacts the quality of the measurements: a misplaced microphone will fail to correctly capture the spatial variations of high frequency sound fields.

In order to guard us against this pitfall, an extended work has been carried out to ensure that the positioning accuracy of the Franka Robotics Panda used for our measurements remains lower than 2 mm (Pascal *et al.*, 2023).

If not completely removed, the actual impact of the remaining positioning errors on acoustic measurements cannot simply be assessed as for the previous hypothesis, and will be considered verified for the time being.

III. THE BOUNDARY ELEMENTS METHOD FOR SOUND FIELD ESTIMATION

Following on the introduction of our robotized acoustic measurement setup, we will now focus on the theoretical background and numerical resolution of the sound field estimation problem using BEM.

A. Previous work

The boundary elements method is a numerical method used to solve partial differential equations, that is particularly well suited for problems where a solution is sought over an infinite domain (Sauter and Schwab, 2011) (Kirkup, 2019). The equations derived from BEM are solely defined on the boundary of the domain. Hence, the solution at any field point can be obtained with no need for a domain wide discretization.

This boundary-wise approach made BEM a perfect candidate for the resolution of the Helmholtz equation in wave scattering problems (Chandler-Wilde *et al.*, 2012), and in NAH (Bai, 1992) (Luo *et al.*, 2019) (Valdivia and Williams, 2004) (Bi *et al.*, 2019) and SFE problems (Kim and Ih, 1996) (Herrin *et al.*, 2010) (Luo *et al.*, 2021). In the latter case, the practical use of BEM with a free-field hypothesis is often hindered by the required boundary conditions, which consist in a set of acoustic measurements performed on closed mesh surrounding the studied source. However, the use of robotized measurements should conveniently ensure the reachability of the targeted mesh nodes.

Most BEM based SFE resolution methods employ colocation techniques (Bai, 1992) (Bi *et al.*, 2019) (Herrin *et al.*, 2010) (Luo *et al.*, 2021), where the boundary integrals are computed by a simple point-wise approximation. If these methods benefits from a simple implementation, and does not require a proper meshing of the measurement surface, it does not take full advantage of BEM variational form.

On the contrary, the *Variational Boundary Element Method* (VBEM) approach (Valdivia and Williams, 2004) (Schuhmacher *et al.*, 2003) (Raveendra *et al.*, 1998), solves NAH problems by increasing BEM discretization complexity both spatially and functionally. First, the boundary surfaces are described using higher order elements, allowing for a better description of the local curvature, and second, the solution is sought using the Galerkin method with Lagrange polynomial elements. Despite its higher computational complexity, this method offers better overall convergence guarantees.

In the remainder of this section, the application of the VBEM to the SFE problem will be detailed, with a particular focus on its theoretical reconstruction errors estimates

B. Problem statement and indirect resolution method

The SFE problem can be formulated as an exterior Dirichlet problem for the Helmholtz equation. We seek a solution of the free-field acoustic equation in the infinite 3D space, knowing its value on a bounded surface.

As pictured on Fig. 5, let us denote by $\partial\Omega$ the surface on which the measurements are performed, and by Ω the exterior domain over which the complex sound field p is studied. Unlike SFT based methods, no particular constraint is set on the shape of $\partial\Omega$, but it must

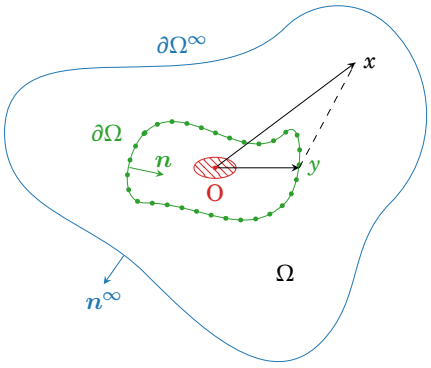

FIG. 5. Dirichlet exterior problem for the Helmholtz equation.

define a smooth closed surface around the studied source. In this situation, the Helmholtz equation, for a constant wave number $k \in \mathbb{R}$, and under the harmonic hypothesis, is written as

$$\begin{cases} \Delta p + k^2 p = 0 & \text{in } \Omega, \\ p = p_0 & \text{on } \partial\Omega, \\ \lim\limits_{\partial\Omega^\infty \to \infty} \left(\frac{\partial}{\partial |x|} - ik \right) p(x) = 0. \end{cases} \tag{1}$$

The infinitely away boundary $\partial\Omega^\infty$ is used to introduce the Sommerfeld radiation condition, which ensures that the solution p is physically acceptable, and that the overall problem is well-posed.

The Green function G associated to Eq. (1) is given by

$$\forall x, y \in \mathbb{R}^3,\ x \neq y,\ G(x,y) = \frac{e^{ik|x-y|}}{4\pi|x-y|}, \tag{2}$$

and allows us to define the single-layer potential S, and double-layer potential D as (Sauter and Schwab, 2011)

$$\forall u : \partial\Omega \to \mathbb{C},\ \forall x \in \mathbb{R}^3 \setminus \partial\Omega,\ S(u)(x) = \int_{\partial\Omega} G(x,y) u(y) d\sigma(y), \tag{3}$$

and

$$\forall u : \partial\Omega \to \mathbb{C},\ \forall x \in \mathbb{R}^3 \setminus \partial\Omega,\ D(u)(x) = \int_{\partial\Omega} \frac{\partial G(x,y)}{\partial \boldsymbol{n}(y)} u(y) d\sigma(y), \tag{4}$$

with u regular enough to be integrated on $\partial\Omega$ and $d\sigma$ defining the surface measure on $\partial\Omega$.

The boundary elements method is then built on the proof that both potentials are infinitely differentiable solutions of Eq. (1) on $\Omega \setminus \partial\Omega$, and the only requirement to extend it over all Ω is to find a boundary density u_S or u_D on $\partial\Omega$ such that the boundary conditions are satisfied. Introducing the Dirichlet trace operator $\gamma_0^{\partial\Omega}$, which extends on $\partial\Omega$ sufficiently smooth functions defined on $\Omega \setminus \partial\Omega$, these problems can be written as

$$\exists\ u_S : \partial\Omega \to \mathbb{C},\ \gamma_0^{\partial\Omega}\left[S(u_S)\right] = V(u_S) = p_0, \tag{5}$$

and

$$\exists\ u_D : \partial\Omega \to \mathbb{C},\ \gamma_0^{\partial\Omega}\left[D(u_D)\right] = \frac{u_D}{2} + K(u_D) = p_0, \tag{6}$$

where V and K denote the *Boundary Integral Operators* (BIOs) arising from the Dirichlet traces of the potentials S and D on $\partial\Omega$.

Both BIOs contain singular surfacic integrals, involving the ill-defined evaluation of the Green function on $\partial\Omega$. Yet, their calculations are still possible but require u_S and u_D to belong in a particular space of functions with sufficient regularity guarantees, and significant computational efforts (*e.g.* specific quadrature formulas for singular integrals computation).

Eventually, Eqs. (5) and (6) define two *Boundary Integral Equations* (BIEs), which can be solved using a Galerkin approximation, where u_S and u_D are sought in a finite dimensional subspace V_h

$$\exists\ u_S \in V_h, \forall v \in V_h,\ \int_{\partial\Omega\times\partial\Omega} V(u_S)(y) v(x) d\sigma(x,y) = \int_{\partial\Omega} p_0(x) v(x) d\sigma(x), \tag{7}$$

and

$$\exists\, u_D \in V_h, \forall v \in V_h,\ \int_{\partial\Omega\times\partial\Omega} \left[\frac{u_D(y)}{2} + K(u_D)(y)\right] v(x) d\sigma(x,y) = \int_{\partial\Omega} p_0(x) v(x) d\sigma(x). \quad (8)$$

The values of u_S (*resp.* u_D) on $\partial\Omega$ are then obtained by solving the fully-populated linear system associated to Eq. (7) (*resp.* Eq. (8)), and can directly be fed to the potential formulations of Eq. (3) (*resp.* Eq. (4)) to reconstruct the sound field p over the whole domain Ω. As the sought quantities are computed using an intermediate potential, this approach of the boundary elements method is often referred to as the indirect formulation.

C. Spurious resonances and hybrid formulations

Even though the single and double layer potentials both provide solutions to Eq. (1), it can be shown that for certain wave numbers, the BIEs Eqs. (7) and (8) are ill-posed, and will not lead to a unique solution (Kreß and Spassov, 1983) (Valdivia, 2019). This phenomenon is known as spurious resonances and is specific to the boundary integral formulation. The issue is either solved by adding over determining equations to the BIEs, as for *Combined Helmholtz Integral Equation Formulation* (CHIEF) method (Schenck, 1968), or by using a hybrid formulation of BEM, combining both the single and double layer potentials (Chandler-Wilde *et al.*, 2012) (Marburg and Wu, 2008)

$$\forall u : \partial\Omega \to \mathbb{C},\ \forall x \in \mathbb{R}^3 \setminus \partial\Omega,\ C(u)(x) = D(u)(x) - i\eta S(u)(x), \quad (9)$$

where η is a complex parameter, chosen equal to the studied wave number k. Applied to the indirect formulation, this combined potential is known as the Brakhage-Werner formulation (Brakhage and Werner, 1965) and has now become a reference in BEM literature. As for

the two other potentials, it provides an infinitely differentiable solution of Eq. (1) on $\Omega \setminus \partial\Omega$, and may be extended on $\partial\Omega$ through the following BIE

$$\exists\, u : \partial\Omega \to \mathbb{C},\ \gamma_0^{\partial\Omega}\left[C(u)\right] = \frac{u}{2} + K(u) - ikV(u) = p_0. \tag{10}$$

Finally, Eq. (10) leads to the Galerkin equation

$$\exists\, u \in V_h, \forall v \in V_h,\ \int_{\partial\Omega\times\partial\Omega} \left[\frac{u(y)}{2} + K(u)(y) - ikV(u)(y)\right] v(x) d\sigma(x,y) = \int_{\partial\Omega} p_0(x) v(x) d\sigma(x), \tag{11}$$

which can be solved for u, and then fed to Eq. (9) to reconstruct the sound field p over the whole domain Ω.

D. Convergence and error estimates

As mentioned earlier, the VBEM approach provides *a priori* error and convergence estimates on the reconstructed sound field. In particular, Sauter and Schwab (2011) focused on the case where the boundary surface is approximated by surface elements of order ℓ (geometric elements), and the solution approximated by Lagrange elements of order m (algebraic elements). As a consequence of the boundary surface approximation, the BIOs are no longer computed on the boundary $\partial\Omega$ itself, but on a mesh of size h, denoted by $\partial\Omega_h$. Introducing Ψ, the orthogonal projector from $\partial\Omega_h$ to $\partial\Omega$, the boundary conditions of Eq. (1) becomes

$$\forall x \in \partial\Omega,\ p(x) = p_{0_h}(x) = p_0\left(\Psi^{-1}(x)\right).$$

Denoting by p the exact solution of Eq. (1) and p_h its computed approximation using the combined and indirect BEM formulation, we have the following convergence behavior

$$\forall y \in \Omega,\ |p(y) - p_h(y)| \lesssim C_A h^{2(m+1)} + C_G h^{\ell} + C_F ||p_0 - p_{0_h}||_{L^2(\partial\Omega)} \tag{12}$$

The estimate given by Eq. (12) shows the crucial impact of geometric approximation on the overall estimation error. For instance, if the surface is approximated by planar triangles, *i.e.*, $\ell = 1$, the estimation error will decrease at worst as fast as $\mathcal{O}(h)$, regardless of the order of Lagrange elements m. The geometric approximation also partially appears in the term involving the difference between the exact and approximated boundary conditions, through the projection operator Ψ. It can be shown (Ciarlet and Raviart, 1972) that this term also decrease with the mesh size, such that

$$||p_0 - p_{0_h}||_{L^2(\partial\Omega)} \lesssim C_R h^{n+1},$$

with n increasing with the regularity of the approximated boundary conditions. In particular, when the boundary conditions are C^{∞}, n is high enough so that this term do not impact the convergence order.

As for the resolution of Eq. (1), the estimate of Eq. (12) is only valid for a given value of the wave number k, which must remain such that $kh \leq 1$ for the result to still hold. This constraint can be viewed as a spatial equivalent of the Shannon criteria: it is not possible to correctly reconstruct a given signal of wavelength λ if it is not spatially sampled at a larger resolution. In practice, this constraint is commonly included by choosing between 3 (Martinus *et al.*, 2007) to 6 (Marburg, 2002) measurements points per studied wavelength.

IV. IMPLEMENTATION AND NUMERICAL SIMULATIONS

As mentioned in previous section, the versatility and convergence guarantees of BEM come at the cost of complex and resources consuming singular integral computations, and dense matrices factorization. However, benefiting from the rise of high performance parallel computing, *FreeFEM++* (Hecht, 2012) proposes a competitive implementation of BEM, relying on the hierarchical matrices' computation tool HTool (Marchand, 2020), and the parallel solvers proposed by PETSc (Balay *et al.*, 1998). Even though *FreeFEM++* handles Lagrange element of order 0 to 2, it currently only supports linear surface elements, hence bounding the expected resolution performances. Despite the limitation identified in subsection III D, the following results were obtained using P_1 Lagrange elements, as they offer a good trade-off between accuracy and computational cost, while allowing for a simplified mesh generation.

A numerical simulation of our BEM based SFE tool was thus implemented in order to assess our implementation agreement with the theoretically expected behaviors, as well as to infer good practices for our measurements setup. This simulation was also used as a mean to evaluate the actual impact of the robotic arm on the estimated acoustic pressure field. The acoustic measurements are simulated using elementary sound sources - the acoustic infinitesimal dipole and regular dipole - whose analytical pressure fields expressions are sampled over a surrounding spheric mesh of varying diameter and size. Each mesh is generated using a geodesic polyhedron primitive to ensure a uniform distribution of the vertices over the sphere.

The estimated sound field is then computed on a circular mesh of diameter 1 m, located in the $z = 0$ plane, and containing 100 nodes, for frequencies distributed between 100 Hz and 5000 Hz. The presented reconstruction errors are defined as the relative L^2 norm between the exact and estimated sound fields, computed over the whole circular mesh

$$\epsilon_{L^2,rel} = \frac{\sum_{i=1}^{N_{\text{nodes}}} \left| p_i^{\text{estimated}} - p_i^{\text{exact}} \right|^2}{\sum_{i=1}^{N_{\text{nodes}}} \left| p_i^{\text{exact}} \right|^2} \tag{13}$$

A. Agreement with theoretical error estimates

Given the choices of geometric and algebraic elements, the convergence rate of the computed solution towards the exact solution is theoretically expected to lay below $\mathcal{O}(h)$. This behavior was confirmed and even superseded by our numerical simulations, as a quadratic convergence rate was actually observed. The corresponding results are shown on on Fig. 6, where the reconstruction error is plotted against the product of the mesh size h and the wave number k.

As was nonetheless expected, the convergence tends to deteriorate when hk nears 10 (Sauter and Schwab, 2011), while the reconstruction error reaches 10 % as hk increases towards 1. Enforcing a maximum estimation error of this magnitude, we indeed fall back on previously mentioned thumb rule of 6 measurements points per wavelength.

This thumb rule turns out to be even more crucial for the regular dipole, whose directivity pattern features sharpening lobes as the frequency increases. In this situation, a finer size mesh h is required to correctly sample the thin spatial variations of the sound field, and to avoid a worn out, smoothed reconstruction as seen on Fig. 7.

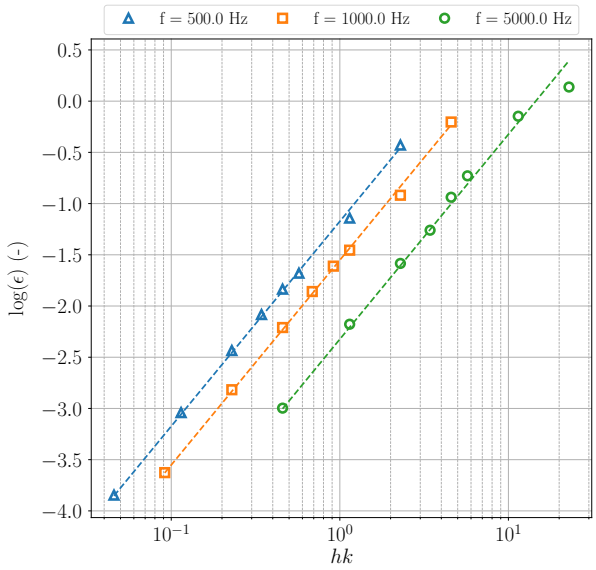

Infinitesimal dipole

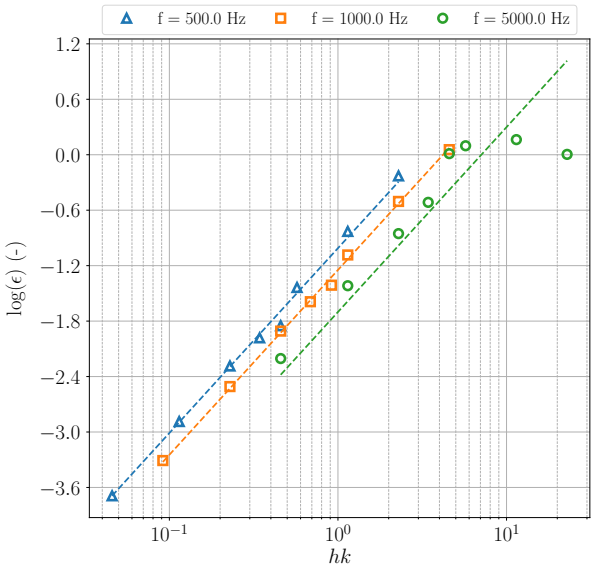

Regular dipole, 0.45 m spacing

FIG. 6. Reconstruction error obtained for measurements performed on a sphere of diameter $D = 0.5$ m, with increasing mesh sizes h. The dashed line represents the actually observed $\mathcal{O}(h^2)$ convergence rate.

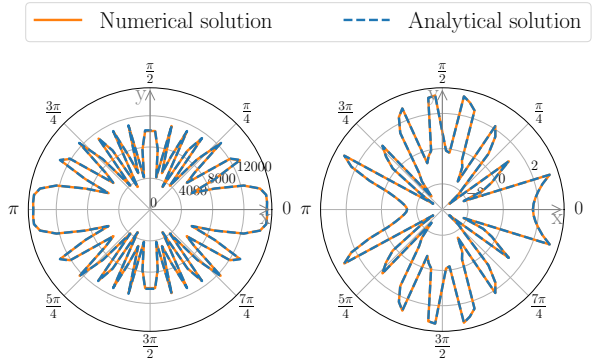

Modulus (Pa) Phase (rad)

Mesh size $h = 0.005$ m - $hk = 0.46$

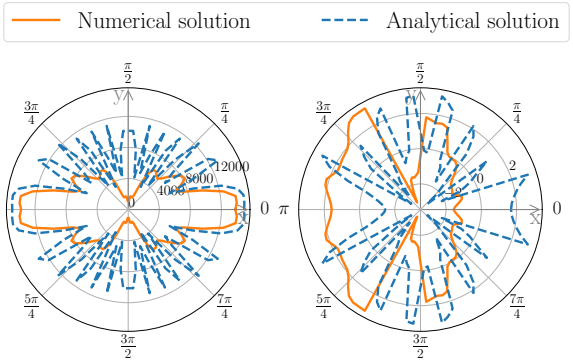

Modulus (Pa) Phase (rad)

Mesh size $h = 0.125$ m - $hk = 11.4$

FIG. 7. Reconstructed directivity pattern obtained at $f = 5$ kHz for measurements of a regular dipole with a 0.45 m spacing performed on a sphere of diameter $D = 0.5$ m.

Despite the numerous advantages of a smaller mesh size, its practical value remains bounded by the minimal distance between two microphones placements, and is *de facto* constrained by the accuracy of the robot. A calibrated robot (Pascal *et al.*, 2023), with smaller positioning errors, will then allow for a finer mesh size, and a better reconstruction of the sound field, as will be further discussed in subsection IV C.

B. Practical guidelines for the measurements setup

Whereas the agreement of our SFE tool with the expected error estimates provided an insight for the measurements density, their distance relative to the studied source remains to be discussed.

Provided that the mesh size satisfies $kh \leq 1$, a larger mesh will provide a more spatially complete sampling of the sound field (Martinus *et al.*, 2007), and eventually reduce the estimation error. This hypothesis was confirmed by our simulations, as seen on figure Fig. 8, with the reconstruction error decreasing with the diameter of the mesh D when the mesh size h remains constant.

Nevertheless, one should bear in mind that this simple numerical simulation does not take into account the physical aspects of real measurements, which heavily depend on the placement of microphones relative to the source. A microphone placed too far from the source will suffer from a high noise to signal ratio, and will be more likely to record reflected sound waves.

In practice, general guidelines (Wu, 2000) advise to place the microphones on surfaces conformal to the studied object (*i.e.*, at a similar distance to the studied object), at a

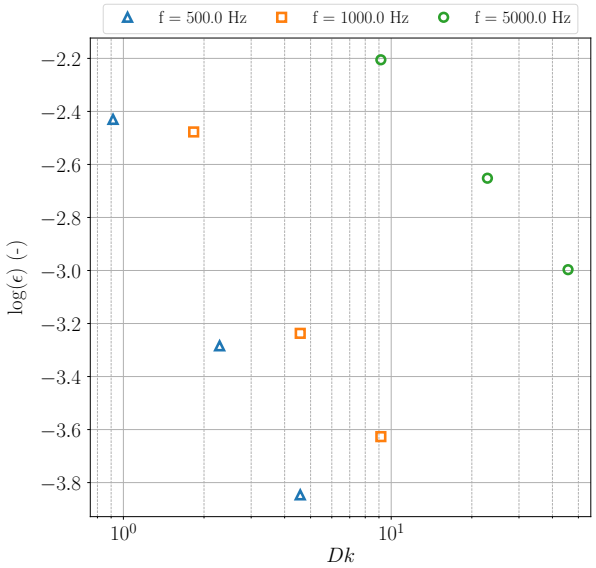

Infinitesimal dipole

FIG. 8. Reconstruction error obtained for measurements performed on spheres of increasing diameters D, with a mesh size $h = 0.005$ mm. The measurements are assumed to be independent of the distance to the sound source.

distance *i*) small in comparison to the studied object and *ii*) small in comparison to the studied wavelength. It is also advised to perform measurements uniformly around the studied source, so that the radiated around field is completely sampled (Martinus *et al.*, 2007).

Finally, from a time-performance point of view, it should be recalled that both the dimensions and size of the measurements mesh directly impact the size of the linear system to solve, and thus the computational cost of the reconstruction algorithm. As shown in Table I, the monitored computation time is found to increase quadratically with the ratio between the diameter of the mesh D and its size h, *i.e.*, linearly with the number of measurements. For the lowest mesh size and highest mesh diameter, the reconstruction of the sought sound field may still take up to several minutes.

TABLE I. Monitored computation times for the reconstruction of the sound field generated by an infinitesimal dipole at 5 kHz, with increasing ratios between the mesh diameter and size $\frac{D}{h}$. Computations were run on the 4 cores of an Intel Core i5-4430 @ 3.00 GHz.

$\frac{D}{h}$	5	10	20	50	100
Computation time (s)	1.80	4.38	16.38	244.46	1664.62

C. Impact of robotized measurements

In section II, we reconned the strong hypothesis that the robot inaccuracies would only have a negligible impact on the acoustic acquisitions, but with no actual measurements to back up this claim. In order to comfort our decision, and to tackle this scarcely address topic, the following section aims to study the impact of a misplacement of the robot on the sound field estimation error.

a. Introducing the robot inaccuracies. The robot positioning inaccuracy is embedded in our simulation in the same way it impacts actual measurements, that is, not by modifying the boundary mesh itself.

Indeed, even with a preliminary calibration, the actual error made by the robot at a given pose cannot be estimated *a posteriori*, and prevents any correction of the boundary mesh. Computations are therefore carried on the theoretical mesh, although the measurements are not exactly performed on the mesh nodes. Consequently, the positioning error is introduced by adding a Gaussian noise of standard deviation σ_P to each coordinate of the points where

the analytical acoustic pressure field is sampled. The obtained noisy measurements are then assigned to the corresponding unmodified mesh elements, as pictured on Fig. 9.

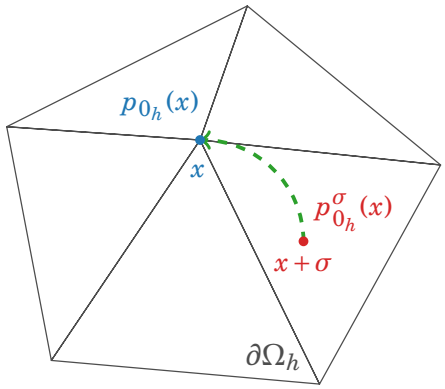

FIG. 9. Illustration of the positioning noise as formulated in Eq. (14). For each node x of the mesh $\partial\Omega_h$, the initial noise-free boundary condition $p_{0_h}(x)$ is replaced by $p^{\sigma}_{0_h}(x)$.

It should be noted that this approach only tackles the position inaccuracies of the robot, and not the orientation ones. In practice, the latter are expected to have a lower impact on the measurements, provided that the deployed microphone maintains the same properties at low incidence angles. In particular, this property is ensured by the Bruel & Kjaer 4190 microphone used in our experimental setup.

The procedure was repeated 20 times for various values of σ_P ranging from $0.1h$ to $2h$, using an infinitesimal dipole as studied source.

b. Impact on the error estimate. Considering our description of the positioning noise, the boundary conditions on $\partial\Omega$ are now given by

$$\begin{aligned} \forall x \in \partial\Omega,\ p(x) = p^{\sigma}_{0_h}(x) &= p^{\sigma}_0\left(\Psi^{-1}(x)\right) \\ &= p_0\left(\Psi^{-1}(x) + \sigma\right) \end{aligned} \tag{14}$$

where σ is a random vector containing three random variables, each following a Gaussian distribution of standard deviation σ_P.

Substituting $p^{\sigma}_{0_h}$ for p_{0_h} in Eq. (12), the error estimate becomes

$$\forall y \in \Omega,\ |p(y) - p_h(y)| \lesssim C_A h^{2(m+1)} + C_G h^{\ell} + C_F ||p_0 - p^{\sigma}_{0_h}||_{L^2(\partial\Omega)} \tag{15}$$

It should be noted that the approximations of p appearing in Eq. (12), p_h, and Eq. (15), p^{σ}_h, are not derived from the same boundary density. Yet, the other terms involved in both estimates remain the same, as the perturbations are added to the measurements directly, and not to the boundary mesh.

Provided that the value of σ_P is small in comparison to the mesh size h and to the wavelength λ, the L^2 norm involving the boundary conditions in Eq. (15) may be approximated by

$$\begin{aligned} ||p_0 - p^{\sigma}_{0_h}||_{L^2(\partial\Omega)} &\simeq ||p_0 - p_{0_h} - \left(\nabla p_0 \circ \Psi^{-1}\right) \cdot \sigma||_{L^2(\partial\Omega)} \\ &\lesssim ||p_0 - p_{0_h}||_{L^2(\partial\Omega)} + |\sigma|||\nabla p_0 \circ \Psi^{-1}||_{L^2(\partial\Omega)}. \end{aligned}$$

The error estimate of Eq. (15) then becomes

$$\begin{aligned} \forall y \in \Omega,\ |p(y) - p_h(y)| \lesssim\ & C_A h^{2(m+1)} + C_G h^{\ell} \\ & + C_F \left(||p_0 - p_{0_h}||_{L^2(\partial\Omega)} + |\sigma|||\nabla p_0 \circ \Psi^{-1}||_{L^2(\partial\Omega)}\right) \end{aligned} \tag{16}$$

with $|\sigma|$ increasing linearly with σ_P.

The last part of the right-hand term of Eq. (16) translates the two-fold impact of placement inaccuracies on the reconstruction error. First, the error will now grow linearly with the value of σ_P, and second, the previously expected $\mathcal{O}(h)$ convergence rate will no longer hold, as the last term does not decrease with the mesh size h anymore.

The two aspects are comforted by the numerical simulations, regarding both the highest and the average estimation errors obtained over the 20 draws. As shown on Fig. 10, these errors are indeed found to broadly follow a linear trend, provided that the values of σ_P remains small in comparison to the mesh size h. The estimation errors obtained with $\sigma_P = 0.0125$ m, which is more than two times the mesh size $h = 0.005$ m, are indeed found to provide off trend results.

For reasonable values of σ_P, but at higher frequencies, the reconstruction error seems to be more sensitive to the value of σ_P as well, with a more likely supra-linear trend. This observation highlights the increasing impact of positioning inaccuracies with the frequency, where a small misplacement of the microphone will lead to a large error in the sampling of the highly spatially varying sound field.

On the other hand, Fig. 11 illustrates the degradation of the convergence rate, by reporting the average slope value of the reconstruction error curve with respect to the mesh size. As expected for both the average and highest estimation errors, the computed values are found to gradually decease from a quadratic trend to a sublinear one as the value of σ_P increases. Here too, the position noise sensitivity at higher frequencies is visible, as the decrease in the corresponding slopes values is seemingly steeper.

Studying the impact of the robot accuracy on the sound field estimation error is also an opportunity to highlight another benefit from a preliminary calibration of the robot (Pascal *et al.*, 2023). Indeed, as shown on Fig. 10, the expected error with an un-calibrated Franka Robotics Panda robot, *i.e.*, $\sigma_P = 7.6$ mm, is on average and in the worst case scenario, almost 4 times higher than the expected error with a calibrated robot, *i.e.*, $\sigma_P = 1.6$ mm. Assuming

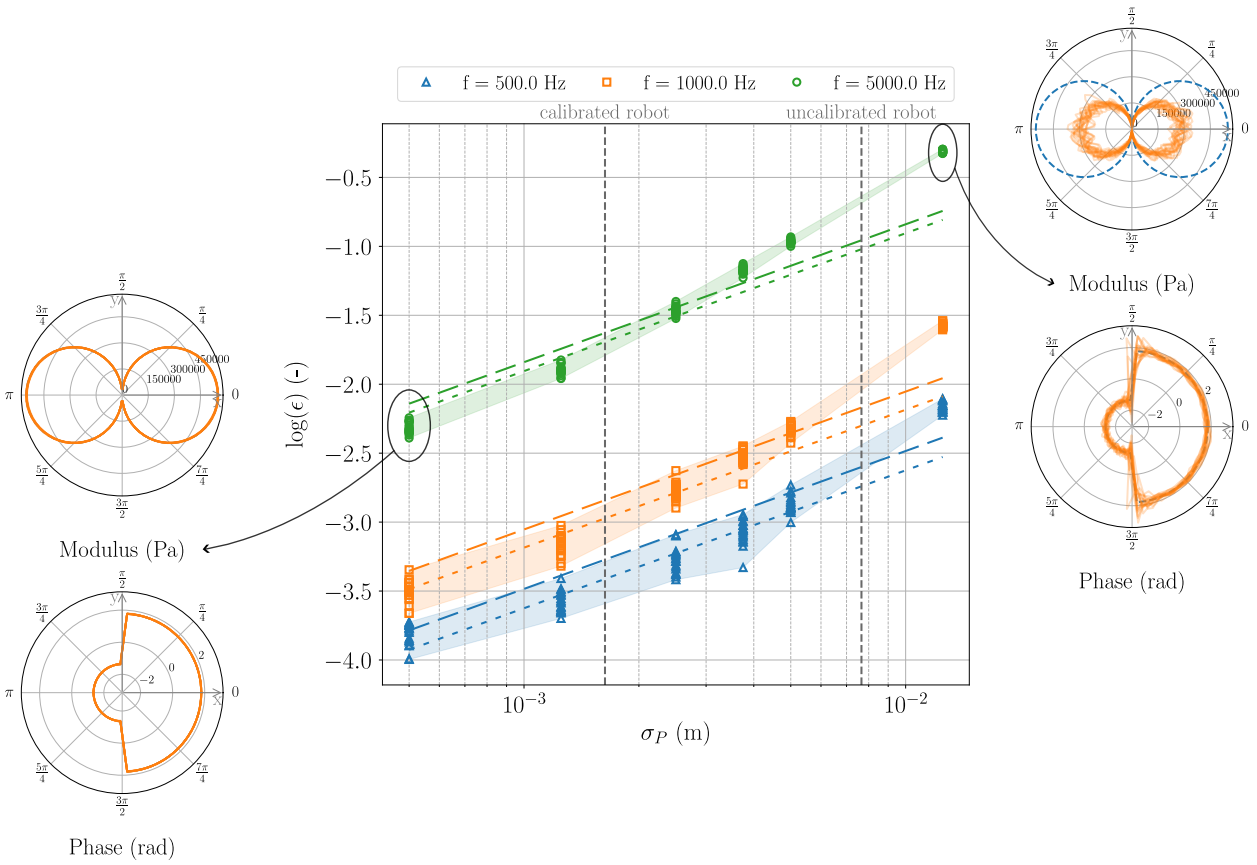

FIG. 10. Reconstruction error obtained for measurements performed on a sphere of diameter 0.5 m with a mesh size of 0.005 m and increasing values of positioning noise σ_P. The dashed and dotted lines represents the expected $\mathcal{O}(\sigma_P)$ convergence rate for the highest and average reconstruction errors, respectively. The directivity patterns illustrate the results of the 20 draws at 5 kHz, for the smallest (left) and largest (right) values of σ_P.

a linear decrease of the reconstruction error with the mesh size h, using a calibrated robot has roughly the same impact as dividing the mesh size by 4.

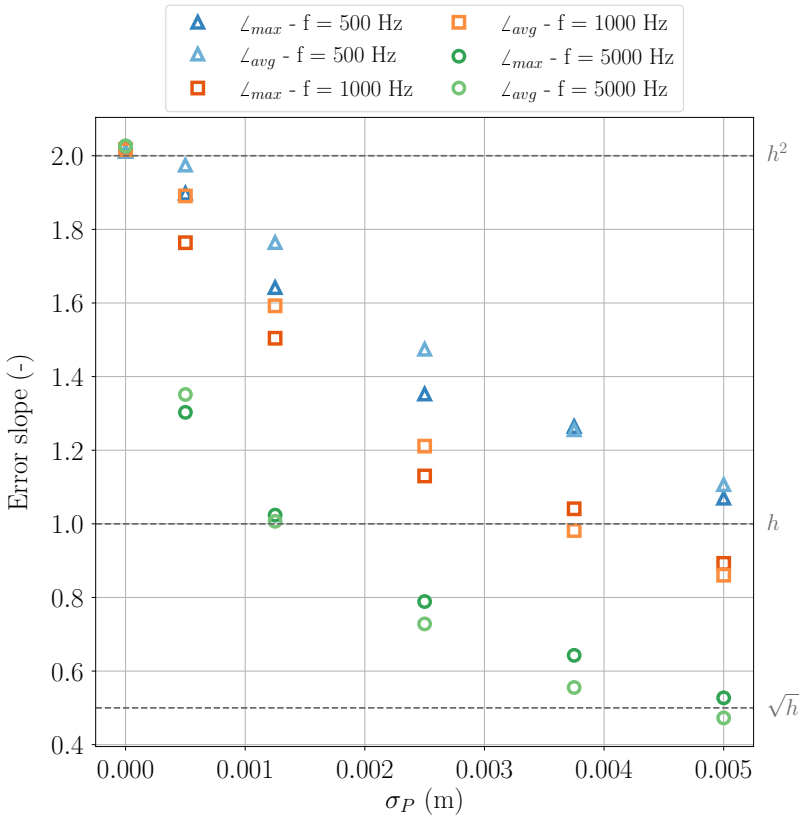

FIG. 11. Evolution of the average slope value of the highest and average reconstruction error curves with respect to the mesh size, for measurements performed on a sphere of diameter 0.5 m and increasing values of σ_P. The dashed lines represent the corresponding quadratic, linear and sublinear trends.

V. EXPERIMENTAL RESULTS

In order to assess the correct operation and performances of our robotized sound field estimation methodology, we applied the complete procedure to the acoustic characterization of an un-modeled JBL Flip 2 loudspeaker.

A. Experimental setup and Robotized measurements

Prior to the deployment of acoustic measurements, and to avoid any collisions between the robot and the loudspeaker, a 3D point cloud of the loudspeaker was recovered using an Intel RealSense D435 depth camera mounted on the robot flange. This point cloud allowed us to extract both a simple geometric description of the loudspeaker for collision avoidance, and its position and orientation relative to the robot base.

Based on the gathered geometric data, and in concordance with the guidelines described in subsection IV B, measurements were planned on a sphere of diameter 0.35 m, centered around the loudspeaker. At its closest point, the microphone will be located at a distance of roughly 0.05 m from the loudspeaker, which is small in comparison to the studied source dimensions, and to the minimal wavelength of the validity range identified in subsection II B, $\lambda_{min} = 0.34$ m. A mesh size of 0.025 m was chosen for the triangulation of the sphere, such that hk remains below 1 over the validity range.

The measurements were then autonomously performed according to the acquisition procedure of section II, by programming the robot to place the microphone successively at each vertex of the mesh, and align it with the local inward normal to the sphere.

Finally, the acquisition was concluded by 20 additional verification measurements, located on a circular mesh of diameter 0.5 cm, lying in the horizontal $z = 0$ plane of the loudspeaker. The total duration as well as the number of measurements are reported in Table II.

TABLE II. Detailled acquisition parameters for the JBL Flip 2 loudspeaker measurements.

Number of mesh vertices	2220
Number of measurements	2153
Missing measurements	3.0%
Overall acquisition duration	16 h 28
Planning & motion duration	9 h 53

It should be noted that the extended acquisition duration is mainly caused by the motion planning computations and executions, which both turned out to be slowed down because of the robot reduced speed, and complex collision avoidance trajectories.

The difference between the actual number of measurements, and the expected number of vertices is mostly caused by collision avoidance with the loudspeaker, or singular, unreachable robot poses. The missing measurements were recovered using an iterative hole-filling procedure, where each missing value is replaced by the averaged data of its direct neighbors. A statistical outliers' removal step was also applied, assuming a normal distribution of the measured phase and amplitude over each vertex direct neighbors.

B. Sound field estimation results

Aiming to assess the conclusions of subsection IV A, two additional meshes were uniformly sub-sampled out of the initial measurements mesh. The detailed features of the three meshes

are reported in Table III, and an outlook of the corresponding measurements is given on Fig. 12.

TABLE III. Details of the three meshes used for the sound field prediction.

	Coarse mesh	**Intermediate mesh**	**Fine mesh**
Size (m)	0.14	0.07	0.025
$\boldsymbol{kh}$ **at 1000** Hz	2.56	1.28	0.46
$\boldsymbol{kh = 1}$ **frequency**	390 Hz	780 Hz	2184 Hz
Number of vertices	54	226	2220

The far-field acoustic pressure field was then estimated with the three measurements sets, using the BEM-based procedure presented in section III and the circular verification mesh as the reconstruction domain. A sample of the detailed results obtained for the three meshes is shown on Fig. 13.

At first sight, the reconstruction seems to correctly fit the measurements, with a faithful rendering of the left monaural directivity pattern of the loudspeaker. However, the SFE appears to have a smoothing effect on both the modulus and phase reconstructions, especially in comparison with the sharper verification measurements. Yet, this observation is not fully reliable, as the varying measurements may also be caused by faulty acquisitions, or by the acoustic perturbations of the robot. Comparing the results obtained with the three meshes, it is actually not clear whether a finer resolution is beneficial, as the reconstructions slightly

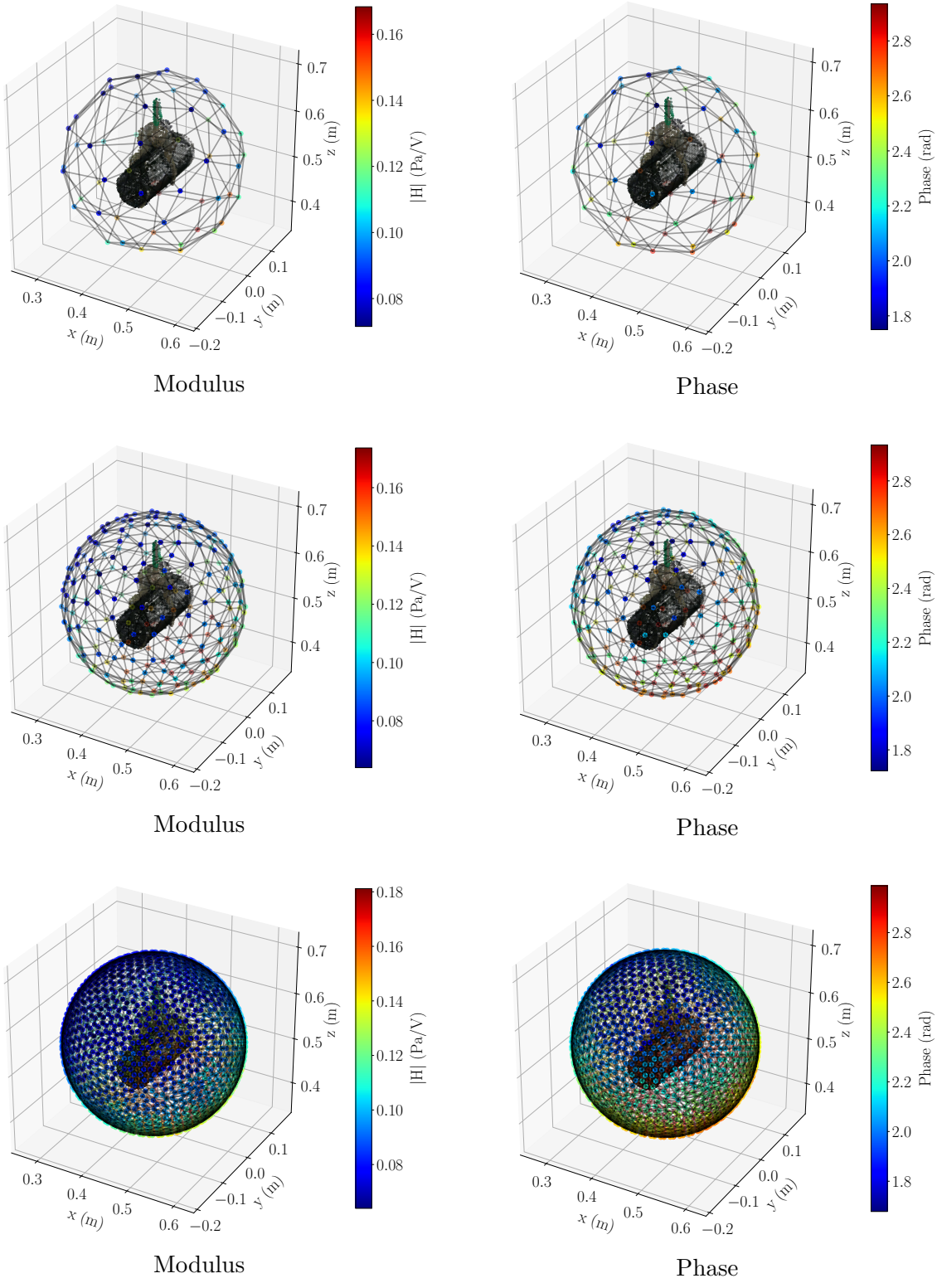

FIG. 12. Example of post-processed measurements at $f = 500$ Hz, for the coarse, intermediate and fine meshes.

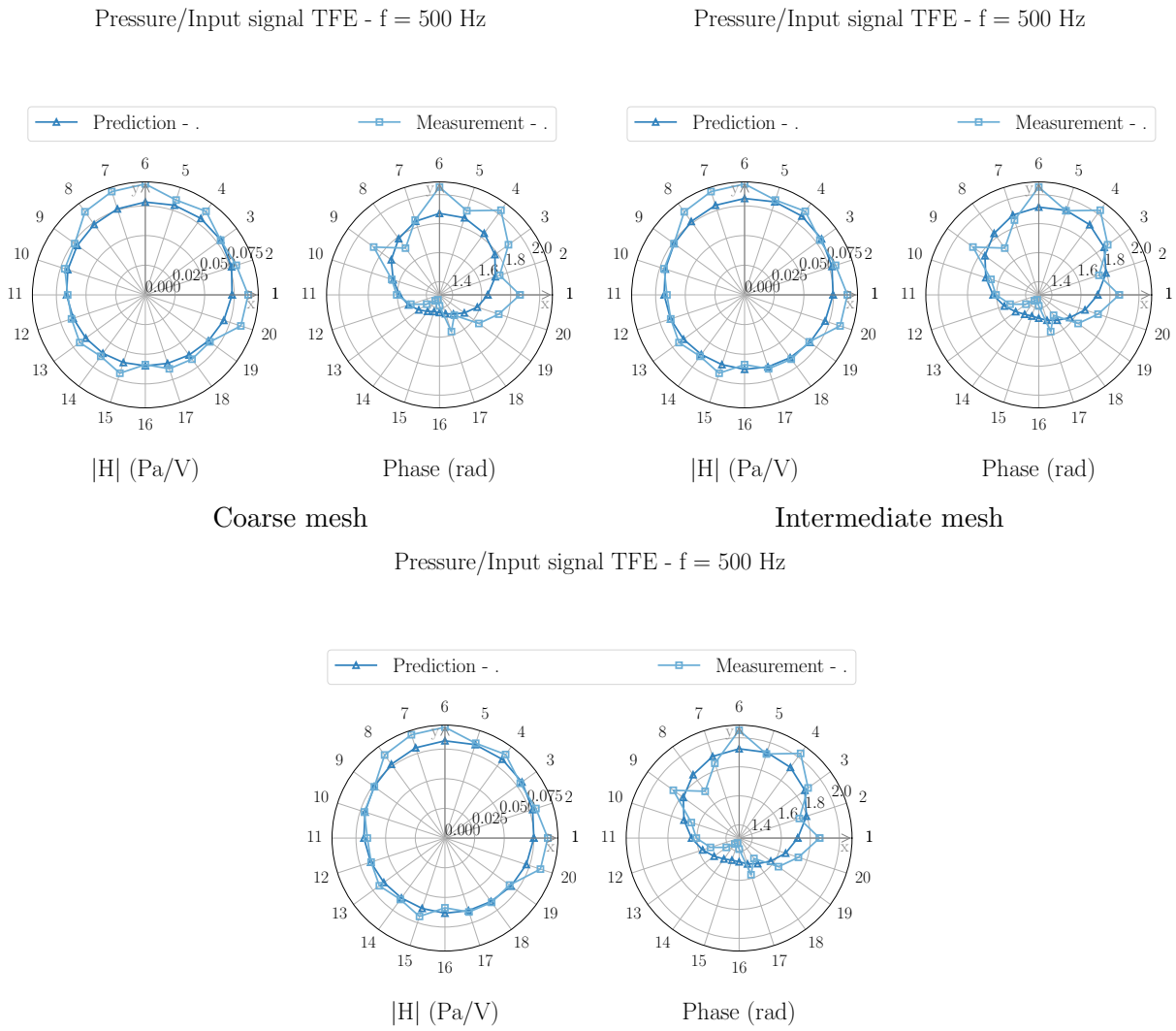

FIG. 13. Predicted and measured acoustic pressure at $f = 500$ Hz, for the coarse, intermediate and fine meshes.

differ from one another, except for the coarse mesh phase prediction, which more clearly undervalued.

Taking a closer look at the evolution of the reconstruction errors with the frequency on Fig. 14, the previous observation is confirmed: the three measurements sets provide very similar results, especially when comparing the intermediate and fine meshes, which are

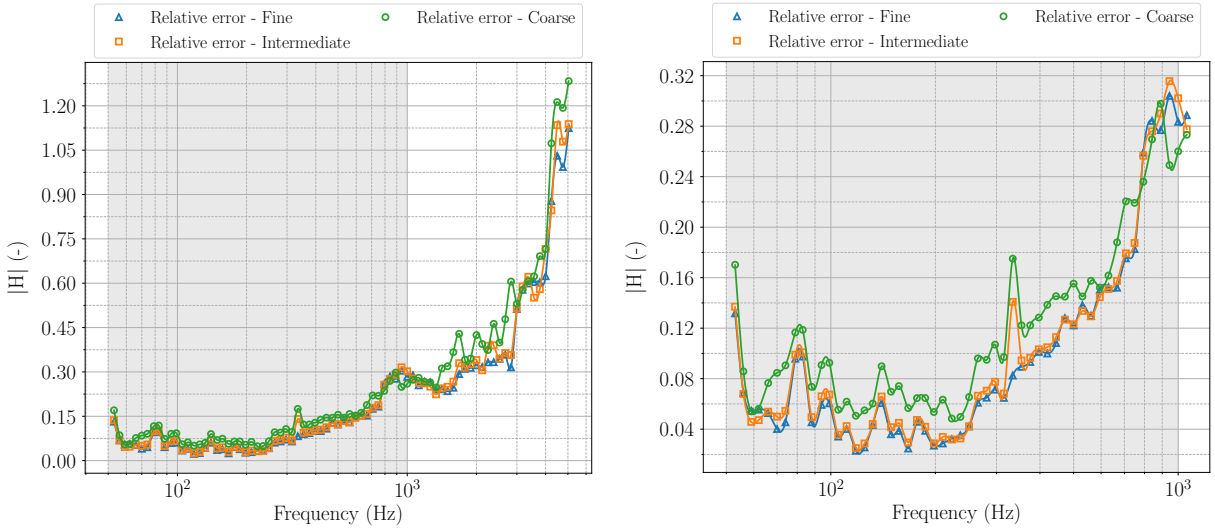

Full frequency range

Validity frequency range (subsection II B)

FIG. 14. Reconstruction error, as defined in Eq. (13), for the coarse, intermediate and fine meshes.

hardly distinguishable, even on the close-up view. The coarse mesh results appear slightly less accurate, whether within or outside the validity frequency range, but the difference still remains far from the predicted 4 times increase for a doubling of the mesh size (*cf.* section IV A).

Considering the fine mesh, and as was expected with measurements performed at a fixed distance form one another, the reconstruction error globally increases with the frequency. In detail, the error remains below 15 % for frequencies below 1 kHz but quickly rise to 30 % around 1 kHz, and towards 100 % when the validity frequency range is outreached, and the frequency reaches 5 kHz. Whereas the explosion of the estimation error at high frequencies, when hk exceeds 1, is in line with the expected behavior of the SFE tool, the sudden increase around 1 kHz is less so. It seems however to match the sharpening impact of the robot acoustic footprint at these frequencies (*cf.* Fig. 4), signaling a weakness in our second hypothesis.

By extension, the ill-compensated acoustic perturbations of the robot, combined with a still perfectible microphone placement could also explain the excessive similarity between the three measurements sets.

TABLE IV. Monitored computation times for the reconstruction of the sound field generated by the JBL Flip 2 at 5 kHz, for the coarse, intermediate and fine meshes. Computations were run on the 4 cores of an Intel Core i5-4430 @ 3.00 GHz.

	Coarse mesh	**Intermediate mesh**	**Fine mesh**
Computation time (s)	1.97	4.51	32.44

In the time being, and considering both the SFE results and the corresponding computation times reported in Table IV, the intermediate mesh seems to provide the best compromise between reconstruction accuracy and computational cost. Yet, the fine mesh is eventually expected to provide more accurate results, granted that the robot acoustic perturbations are properly accounted for.

VI. FUTURE WORK AND CONCLUSION

Throughout this paper, we tackled the problem of sound field estimation considering both the measurements and reconstruction aspects. The requirements for spatially dense and versatile acoustic measurements were met using a robotic arm, which also allows for a fully autonomous acquisition of the data. The impact of the robot on the measurements

was assessed, and found to be acceptable provided that the studied source is sufficiently repeatable, the robot properly calibrated, and the studied frequencies remain below 1 kHz.

The reconstruction was performed using a resonance-free VBEM-based method, benefiting from *FreeFEM++* parallelization capabilities. This approach was found to be computationally efficient, and to provide accurate results, as the expected reconstruction error decreases quadratically with the mesh size, and linearly with the number of measurements. The estimation errors caused by the robot positioning inaccuracies were also studied, and despite lowering the expected convergence rate to the square root of the mesh size, their impact was found to remain acceptable thanks to the robot calibration.

The overall procedure was finally tested on a JBL Flip 2 loudspeaker, around which more than 2000 measurements were autonomously performed in less than 17 hours. The estimated acoustic pressure was found to be in good agreement with the measured data, with a reconstruction error below 30% for frequencies below 1 kHz. However, the expected quadratic increase in the estimation error with the measurements spacing was not clearly observed, and erratic behaviors were noticed around 1 kHz, where the robot acoustic perturbations reach significant levels.

a. Perspectives in robotized acoustic measurements and sound field estimation. As mentioned in subsection V B, the deviation of experimental results from theoretical expectations highlights a failure in our hypothesis, especially regarding the robot acoustic footprint. In this matter, both physical and numerical solutions can be considered.

On one hand, the application of foam on the robot surface could help dampen reflections at high frequencies, while increasing the distance between the robot body and the studied

source during the acquisition could also reduce the amplitude of the reflected waves. Following the general guidelines provided by Wu (2000) and Martinus *et al.* (2007), building a measurement mesh close and conformal to the studied object should also help to reduce the noise to signal ratio.

On the other hand, filtering techniques such as the wave separation method, or the time windowing technique (Klippel, 2022), should be able to partially remove the robot perturbations, thanks to additional, but easily performed measurements. In particular, (Gao *et al.*, 2022) (Langrenne *et al.*, 2008) investigated promising BEM based implementations of the wave separation method, using double layered measurements.

Concluding on the SFE part, *FreeFEM++* BEM implementation presented in section IV, could evidently benefit from the use of higher surface elements, which would allow to take the full benefits from higher order Lagrange elements. Furthermore, deepening the possibilities offered by PETSc (Balay *et al.*, 1998), the use of the minimization based solvers makes us confident in the possibility to tackle SFE dual NAH problem, whose inverse-problem nature might help to reduce SFE smoothing effect.

On a more theoretical level, the quadratic convergence rates observed in our simulations call for a sharper reconstruction error estimate than Eq. (12), which could benefit from the finer geometric arguments of Nedelec (1976).

ACKNOWLEDGMENTS

Authors warmly thanks Thibault Toralba and Clément Yver, and Clément Savaro for their help setting up the robotized measurements setup.

This work was partially supported by Carnot TSN, Carnot Mines, and *Agence de l'Innovation de Défense* – AID – via *Centre Interdisciplinaire d'Études pour la Défense et la Sécurité* – CIEDS – (project 2022 - *Aéroacoustique des systèmes multi-PROpulseurs pour les drones* (APRO)).

Alguacil, A., Bauerheim, M., Jacob, M. C., and Moreau, S. (**2021**). "Predicting the propagation of acoustic waves using deep convolutional neural networks," Journal of Sound and Vibration **512**, 116285, doi: 10.1016/j.jsv.2021.116285.

Antoni, J. (**2012**). "A bayesian approach to sound source reconstruction: Optimal basis, regularization, and focusing," The Journal of the Acoustical Society of America **131**(4), 2873–2890, doi: 10.1121/1.3685484.

Bai, M. R. (**1992**). "Application of bem (boundary element method)-based acoustic holography to radiation analysis of sound sources with arbitrarily shaped geometries," The Journal of the Acoustical Society of America **92**(1), 533–549, doi: 10.1121/1.404263.

Balay, S., Gropp, W., McInnes, L. C., and Smith, B. F. (**1998**). "Petsc, the portable, extensible toolkit for scientific computation," Argonne National Laboratory **2**(17).

Behler, G., Pollow, M., and Vorländer, M. (**2012**). "Measurements of musical instruments with surrounding spherical arrays," in *Acoustics 2012*, Nantes, France.

Bernhardt, Y., Solodov, D., Müller, D., and Kreutzbruck, M. (**2020**). "Listening for airborne sound of damage: A new mode of diagnostic imaging," Frontiers in Built Environment **6**, doi: 10.3389/fbuil.2020.00066.

Bi, C.-X., Liu, Y., Zhang, Y.-B., and Xu, L. (**2019**). "Sound field reconstruction using inverse boundary element method and sparse regularization," The Journal of the Acoustical Society of America **145**(5), 3154–3162, doi: 10.1121/1.5109393.

Bi, H., Ma, F., Abhayapala, T. D., and Samarasinghe, P. N. (**2021**). "Spherical array based drone noise measurements and modelling for drone noise reduction via propeller phase control," in *2021 IEEE Workshop on Applications of Signal Processing to Audio and Acoustics (WASPAA)*, New Paltz, NY, USA, pp. 286–290, doi: 10.1109/WASPAA52581.2021.9632719.

Brakhage, H., and Werner, P. (**1965**). "Über das dirichletsche außenraumproblem für die helmholtzsche schwingungsgleichung," Archiv der Mathematik **16**(1), 325–329, doi: 10.1007/BF01220037.

Canclini, A., Varini, M., Antonacci, F., and Sarti, A. (**2017**). "Dictionary-based equivalent source method for near-field acoustic holography," in *2017 IEEE International Conference on Acoustics, Speech and Signal Processing (ICASSP)*, New Orleans, LA, USA, pp. 166–170, doi: 10.1109/ICASSP.2017.7952139.

Chandler-Wilde, S. N., Graham, I. G., Langdon, S., and Spence, E. A. (**2012**). "Numerical-asymptotic boundary integral methods in high-frequency acoustic scattering," Acta Numerica **21**, 89–305, doi: 10.1017/S0962492912000037.

Chardon, G., Cohen, A., and Daudet, L. (**2013**). "Reconstruction of solutions to the helmholtz equation from punctual measurements," in *10th International Conference on Sampling Theory and Applications (SampTA 2013)*, Bremen, Germany, pp. 164–167.

Chardon, G., Daudet, L., Peillot, A., Ollivier, F., Bertin, N., and Gribonval, R. (**2012**). "Near-field acoustic holography using sparse regularization and compressive sampling principles," The Journal of the Acoustical Society of America **132**(3), 1521–1534, doi: 10.1121/1.4740476.

Chen, X., Ma, F., Bastine, A., Samarasinghe, P., and Sun, H. (**2023**). "Sound field estimation around a rigid sphere with physics-informed neural network," in *2023 Asia Pacific Signal and Information Processing Association Annual Summit and Conference (APSIPA ASC)*, Taipei, Taiwan, pp. 1984–1989, doi: 10.1109/APSIPAASC58517.2023.10317164.

Ciarlet, P. G., and Raviart, P. A. (**1972**). "Interpolation theory over curved elements, with applications to finite element methods," Computer Methods in Applied Mechanics and Engineering **1**(2), 217–249, doi: 10.1016/0045-7825(72)90006-0.

Coleman, D., Sucan, I. A., Chitta, S., and Correll, N. (**2014**). "Reducing the barrier to entry of complex robotic software: A moveit! case study," Journal on Software Engineering for Robotics **5**(1), 3–16, doi: 10.6092/JOSER_2014_05_01_p3.

De La Croix, D. V., Le Sueur, B., and Isnard, N. (**2005**). "Productive measurement of transmission loss characteristics using nearfield acoustic holography," in *SAE Brasil 2005 Congress and Exhibit*, Sao Paulo , Brazil, doi: 10.4271/2005-01-4166.

Doaré, O. (**2024**). "measpy" https://github.com/odoare/measpy.

Fernandez Comesana, D., Steltenpool, S., Korbasiewicz, M., and Tijs, E. (**2015**). "Direct acoustic vector field mapping: New scanning tools for measuring 3d sound intensity in 3d space," in *Proceedings of the 10th European Conference on Noise Control, Euronoise 2015*, Maastricht, Netherlands.

660 Gade, S., Gomes, J., and Hald, J. (**2014**). "Using hand-held arrays for automotive nvh
661 measurements," Sound and Vibration **48**, 12–16.
662 Gao, H., Zhu, Q., Liu, S., Xing, P., and Li, G. (**2022**). "The formulations based on the
663 indirect boundary element method for the acoustic characterization of an arbitrarily shaped
664 source in a bounded noisy environment," Engineering Analysis with Boundary Elements
665 **138**, 65–82, doi: 10.1016/j.enganabound.2022.01.021.
666 Gur, B. (**2014**). "Particle velocity gradient based acoustic mode beamforming for short
667 linear vector sensor arrays," The Journal of the Acoustical Society of America **135**(6),
668 3463–3473, doi: 10.1121/1.4876180.
669 Gur, B. (**2017**). "Modal beamforming for small circular arrays of particle velocity sensors,"
670 in *2017 25th European Signal Processing Conference (EUSIPCO)*, Kos island, Greece, pp.
671 390–394, doi: 10.23919/EUSIPCO.2017.8081235.
672 Hald, J. (**2009**). "Basic theory and properties of statistically optimized near-field acoustical
673 holography," The Journal of the Acoustical Society of America **125**(4), 2105–2120, doi:
674 10.1121/1.3079773.
675 Hald, J. (**2016**). "Fast wideband acoustical holography," The Journal of the Acoustical
676 Society of America **139**(4), 1508–1517, doi: 10.1121/1.4944757.
677 Hald, J. (**2018**). "A comparison of iterative sparse equivalent source methods for near-field
678 acoustical holography," The Journal of the Acoustical Society of America **143**(6), 3758–
679 3769, doi: 10.1121/1.5042223.
680 Hald, J., Mørkholt, J., Hardy, P., Trentin, D., Bach-Andersen, M., and Keith, G. (**2008**).
681 "Array based measurement of radiated and absorbed sound intensity components," The

Journal of the Acoustical Society of America **123**(5_Supplement), 3387, doi: 10.1121/1.2934043.

Havranek, Z., Benes, P., and Klusacek, S. (**2015**). "Application of mems microphone array for acoustic holography," in *Proceedings of the 10th European Conference on Noise Control, Euronoise 2015*, Maastricht, Netherlands, pp. 919–924.

Hecht, F. (**2012**). "New development in freefem++," Journal of Numerical Mathematics **20**(3-4), 251–265.

Herrin, D. W., Liu, J., Martinus, F., Kato, D. J., and Cheah, S. (**2010**). "Prediction of sound pressure in the far field using the inverse boundary element method," Noise Control Engineering Journal **58**(1), 74–82, doi: 10.3397/1.3220625.

Kefer, M., and Lu, Q. (**2016**). "Acoustic holography — a robot application," in *2016 IEEE International Conference on Real-time Computing and Robotics (RCAR)*, Angkor Wat, Cambodia, pp. 312–316, doi: 10.1109/RCAR.2016.7784045.

Kim, B.-K., and Ih, J.-G. (**1996**). "On the reconstruction of the vibro-acoustic field over the surface enclosing an interior space using the boundary element method," The Journal of the Acoustical Society of America **100**(5), 3003–3016, doi: 10.1121/1.417112.

Kirkup, S. (**2019**). "The boundary element method in acoustics: A survey," Applied Sciences **9**(8), 1642, doi: 10.3390/app9081642.

Klippel, W. (**2022**). "Modeling and testing of loudspeakers used in sound-field control," in *Advances in Fundamental and Applied Research on Spatial Audio* (IntechOpen).

Klippel, W., and Bellmann, C. (**2016**). "Holographic nearfield measurement of loudspeaker directivity," in *141st Audio Engineering Society International Convention*, Los Angeles,

CA, USA.

Knežević, N., Bjelić, M., and Jovanović, K. (**2018**). "Automated sound intensity measurement with robot and intensity probe," International Journal of Electrical Engineering and Computing **2**(1), 20–28, doi: 10.7251/IJEEC1801020K.

Kreß, R., and Spassov, W. T. (**1983**). "On the condition number of boundary integral operators for the exterior dirichlet problem for the helmholtz equation," Numerische Mathematik **42**(1), 77–95, doi: 10.1007/BF01400919.

Langrenne, C., Melon, M., and Garcia, A. (**2008**). "A boundary element method for near-field acoustical holography in bounded noisy environment," The Journal of the Acoustical Society of America **123**(5_Supplement), 3309, doi: 10.1121/1.2933747.

Legg, M., and Bradley, S. (**2013**). "A combined microphone and camera calibration technique with application to acoustic imaging," IEEE Trans. on Image Process. **22**(10), 4028–4039, doi: 10.1109/TIP.2013.2268974.

Legg, M., and Bradley, S. (**2014**). "Automatic 3d scanning surface generation for microphone array acoustic imaging," Applied Acoustics **76**, 230–237, doi: 10.1016/j.apacoust.2013.08.008.

Li, D., Wu, H., Zha, Y., and Jiang, W. (**2021**). "A sound source reconstruction approach based on the machine vision and inverse patch transfer functions method," Applied Acoustics **181**, 108180, doi: 10.1016/j.apacoust.2021.108180.

Luo, Z.-W., Fernandez Comesana, D., Zheng, C.-J., and Bi, C.-X. (**2019**). "Near-field acoustic holography with three-dimensional scanning measurements," Journal of Sound and Vibration **439**, 43–55, doi: 10.1016/j.jsv.2018.09.049.

Luo, Z.-W., Fernandez Comesana, D., Zheng, C.-J., and Bi, C.-X. (**2021**). "A free field recovery technique based on the boundary element method and three-dimensional scanning measurements," The Journal of the Acoustical Society of America **150**(5), 3929–3948, doi: 10.1121/10.0007285.

Marburg, S. (**2002**). "Six boundary elements per wavelength: Is that enough?," Journal of Computational Acoustics **10**, 25–51, doi: 10.1142/S0218396X02001401.

Marburg, S., and Wu, T.-W. (**2008**). "Treating the phenomenon of irregular frequencies," in *Computational Acoustics of Noise Propagation in Fluids - Finite and Boundary Element Methods*, edited by S. Marburg and B. Nolte (Springer, Berlin, Heidelberg), pp. 411–434, doi: 10.1007/978-3-540-77448-8_16.

Marchand, P. (**2020**). "Schwarz methods and boundary integral equations," Theses, Sorbonne Université.

Martinus, F., Herrin, D., Tao, Z., and Seybert, A. (**2005**). "Identification of aeroacoustic noise sources using inverse boundary element method," in *SAE 2005 Noise and Vibration Conference and Exhibition*, doi: 10.4271/2005-01-2497.

Martinus, F., Herrin, D. W., and Seybert, A. F. (**2007**). "Selecting measurement locations to minimize reconstruction error using the inverse boundary element method," J. Comp. Acous. **15**(04), 531–555, doi: 10.1142/S0218396X07003482.

Maynard, J. D., Williams, E. G., and Lee, Y. (**1985**). "Nearfield acoustic holography: I. theory of generalized holography and the development of nah," The Journal of the Acoustical Society of America **78**(4), 1395–1413, doi: 10.1121/1.392911.

McBride, S., Motaharibidgoli, S., Albakri, M., Burdisso, R., Tarazaga, P., and Sandu, C. (**2020**). "Experimental study on tire vibrations and induced noise," in *Topics in Modal Analysis & Testing, Volume 8*, edited by M. L. Mains and B. J. Dilworth (Springer International Publishing), pp. 327–332, doi: 10.1007/978-3-030-12684-1_34.

Meyer, A., and Döbler, D. (**2006**). "Noise source localization within a car interior using 3d-microphone arrays," in *Berlin Beamforming Conference (BeBeC) 2006*, Berlin, Germany.

Nedelec, J. C. (**1976**). "Curved finite element methods for the solution of singular integral equations on surfaces in r3," Computer Methods in Applied Mechanics and Engineering **8**(1), 61–80, doi: 10.1016/0045-7825(76)90053-0.

Nolan, M., Verburg, S. A., Brunskog, J., and Fernandez-Grande, E. (**2019**). "Experimental characterization of the sound field in a reverberation room," The Journal of the Acoustical Society of America **145**(4), 2237–2246, doi: 10.1121/1.5096847.

Norris, A. N. (**1997**). "Far-field acoustic holography onto cylindrical surfaces using pressure measured on semicircles," The Journal of the Acoustical Society of America **102**(4), 2098–2107, doi: 10.1121/1.419591.

Olivieri, M., Pezzoli, M., Antonacci, F., and Sarti, A. (**2021**). "A physics-informed neural network approach for nearfield acoustic holography," Sensors **21**(23), 7834, doi: 10.3390/s21237834.

Pascal, C. (**2024**). "robot_arm_acoustic" https://gitlab.ensta.fr/pascal.2020/robot_arm_acoustic.

Pascal, C., Chapoutot, A., and Doaré, O. (**2023**). "A ros-based kinematic calibration tool for serial robots," in *2023 IEEE/RSJ International Conference on Intelligent Robots and*

Systems (IROS), Detroit, MI, USA.

Quigley, M., Conley, K., Gerkey, B., Faust, J., Foote, T., Leibs, J., Wheeler, R., Ng, A. Y. *et al.* (**2009**). "Ros: An open-source robot operating system," in *ICRA Workshop on Open Source Software*, Kobe, Japan, Vol. 3, p. 5.

Raveendra, S. T., Vlahopoulos, N., and Glaves, A. (**1998**). "An indirect boundary element formulation for multi-valued impedance simulation in structural acoustics," Applied Mathematical Modelling **22**(6), 379–393, doi: 10.1016/S0307-904X(98)10013-6.

Salin, M. B., and Kosteev, D. A. (**2020**). "Nearfield acoustic holography-based methods for far field prediction," Applied Acoustics **159**, 107099, doi: 10.1016/j.apacoust.2019.107099.

Sauter, S. A., and Schwab, C. (**2011**). *Boundary Element Methods*, **39** of *Springer Series in Computational Mathematics* (Springer, Berlin, Heidelberg).

Schenck, H. A. (**1968**). "Improved integral formulation for acoustic radiation problems," The Journal of the Acoustical Society of America **44**(1), 41–58, doi: 10.1121/1.1911085.

Schuhmacher, A., Hald, J., Rasmussen, K. B., and Hansen, P. C. (**2003**). "Sound source reconstruction using inverse boundary element calculations," The Journal of the Acoustical Society of America **113**(1), 114–127, doi: 10.1121/1.1529668.

Semenova, T., and Wu, S. F. (**2005**). "On the choice of expansion functions in the helmholtz equation least-squares method," The Journal of the Acoustical Society of America **117**(2), 701–710, doi: 10.1121/1.1841591.

Shigemi, K., Koyama, S., Nakamura, T., and Saruwatari, H. (**2022**). "Physics-informed convolutional neural network with bicubic spline interpolation for sound field estimation,"

in *2022 International Workshop on Acoustic Signal Enhancement (IWAENC)*, Bamberg, Germany, pp. 1–5, doi: 10.1109/IWAENC53105.2022.9914792.

Su, J. B., Wang, C. M., and Xiao, Y. J. (**2017**). "Reconstructing the acoustic far-field using a semi-circular sensor array," Vibroengineering Procedia **14**, 278–282, doi: 10.21595/vp.2017.19190.

Sugiyama, C., Itoyama, K., Nishida, K., and Nakadai, K. (**2023**). "Assessment of simultaneous calibration for positions, orientations, and time offsets in multiple microphone arrays systems," in *2023 IEEE/SICE International Symposium on System Integration (SII)*, Atlanta, GA, USA, pp. 1–6, doi: 10.1109/SII55687.2023.10039440.

Szczodrak, M., Kurowski, A., Kotus, J., Czyżewski, A., and Kostek, B. (**2016**). "A system for acoustic field measurement employing cartesian robot," Metrology and Measurement Systems **23**(3), 333–343, doi: 10.1515/mms-2016-0037.

Tao, Z., and Ren, Y. (**2010**). "Application of inverse boundary element method for far field sound pressure prediction of a diesel engine," SAE Int. J. Commer. Veh. **3**(1), 216–220, doi: 10.4271/2010-01-1984.

Ungnad, S., and Sachau, D. (**2019**). "Interior near-field acoustic holography based on finite elements," The Journal of the Acoustical Society of America **146**(3), 1758–1768, doi: 10.1121/1.5126513.

Valdivia, N., and Williams, E. (**2004**). "Implicit methods of solution to integral formulations in boundary element method based nearfield acoustic holography," Acoustical Society of America Journal **116**, 1559–1572, doi: 10.1121/1.1777854.

Valdivia, N. P. (**2019**). "Advanced equivalent source methodologies for near-field acoustic holography," Journal of Sound and Vibration **438**, 66–82, doi: 10.1016/j.jsv.2018.08.028.

Virovlyansky, A. L., and Deryabin, M. S. (**2019**). "On the use of the equivalent source method for free-field calibration of an acoustic radiator in a reverberant tank," Journal of Sound and Vibration **455**, 69–81, doi: 10.1016/j.jsv.2019.05.018.

Vold, H., Shah, P., Davis, J., Bremner, P., McLaughlin, D., Morris, P., Veltin, J., and McKinley, R. (**2010**). "High resolution continuous scan acoustical holography applied to high-speed jet noise," in *16th AIAA/CEAS Aeroacoustics Conference*, Stockholm, Sweden.

Walker, J., and Foged, I. W. (**2018**). "Robotic methods in acoustics: Analysis and fabrication processes of sound scattering acoustic panels," in *36th eCAADe Conference*, Lodz, Poland, Vol. 1, pp. 835–840.

Wang, R., and Bei, S. (**2017**). "Optimization of fixed microphone array in high speed train noises identification based on far-field acoustic holography," Advances in Acoustics and Vibration **2017**, e1894918, doi: 10.1155/2017/1894918.

Welch, P. (**1967**). "The use of fast fourier transform for the estimation of power spectra: A method based on time averaging over short, modified periodograms," IEEE Transactions on Audio and Electroacoustics **15**(2), 70–73, doi: 10.1109/TAU.1967.1161901.

Williams, E. G. (**2001**). "Regularization methods for near-field acoustical holography," The Journal of the Acoustical Society of America **110**(4), 1976–1988, doi: 10.1121/1.1404381.

Wu, S. F. (**2000**). "On reconstruction of acoustic pressure fields using the helmholtz equation least squares method," The Journal of the Acoustical Society of America **107**(5), 2511–

834 2522, doi: 10.1121/1.428639.

835 Wu, S. F. (**2015**). "The helmholtz equation least-squares method," in *The Helmholtz Equa-*
836 *tion Least Squares Method: For Reconstructing and Predicting Acoustic Radiation*, edited
837 by S. F. Wu, Modern Acoustics and Signal Processing (Springer, New York, NY, USA),
838 pp. 27–62, doi: 10.1007/978-1-4939-1640-5_3.

839 Wu, S. F., and Wu, Y. (**1998**). "Reconstruction of radiated acoustic pressure fields from
840 a complex vibrating structure," in *ASME 1998 International Mechanical Engineering*
841 *Congress and Exposition*, American Society of Mechanical Engineers Digital Collection,
842 pp. 339–345, doi: 10.1115/IMECE1998-0528.